

The kinematics and plasma properties of a solar surge triggered by chromospheric activity in AR11271.

[Download Here](#)



IOPscience

THE ASTROPHYSICAL JOURNAL

THE KINEMATICS AND PLASMA PROPERTIES OF A SOLAR SURGE TRIGGERED BY CHROMOSPHERIC ACTIVITY IN AR11271

P. Kayshap^{1,2}, Abhishek K. Srivastava¹, and K. Murawski²

Published 2012 December 28 • © 2013. The American Astronomical Society. All rights reserved.

[The Astrophysical Journal, Volume 763, Number 1](#)



[Article PDF](#)

2180 Total downloads

[Cited by 8 articles](#)

[Get permission to re-use this article](#)

Share this article



+ Article information

Author e-mails

kmur@kft.umcs.lublin.pl

Author affiliations

¹ Aryabhatta Research Institute of Observational Sciences (ARIES), Manora Peak,

Nainital 263 129, India

² Group of Astrophysics, UMCS, ul. Radziszewskiego 10, 20-031 Lublin, Poland

Dates

Received 2012 June 27

Accepted 2012 November 13

Published 2012 December 28

Citation

P. Kayshap *et al.* 2013 *ApJ* **763** 24

 Create citation alert

DOI

<https://doi.org/10.1088/0004-637X/763/1/24>

Keywords

[magnetohydrodynamics \(MHD\)](#) ; [Sun: chromosphere](#); [Sun: corona](#)

 Journal RSS feed

 Sign up for new issue notifications

Abstract

We observe a solar surge in NOAA AR11271 using the *Solar Dynamics Observatory (SDO)* Atmospheric Imaging Assembly 304 Å image data on 2011 August 25. The surge rises vertically from its origin up to a height of \approx 65 Mm with a terminal velocity of \approx 100 km s⁻¹, and thereafter falls and fades gradually. The total lifetime of the surge was \approx 20 minutes. We also measure the temperature and density distribution of the observed surge during its maximum rise and find an average temperature and a density of 2.0 MK and 4.1×10^9 cm⁻³, respectively. The temperature map shows the expansion and mixing of cool plasma lagging behind the hot coronal plasma along the surge. Because *SDO/HMI* temporal image data do not show any detectable evidence of significant photospheric magnetic field cancellation for the formation of the observed surge, we infer that it is probably driven by magnetic-reconnection-

generated thermal energy in the lower chromosphere. The radiance (and thus the mass density) oscillations near the base of the surge are also evident, which may be the most likely signature of its formation by a reconnection-generated pulse. In support of the present observational baseline of the triggering of the surge due to chromospheric heating, we devise a numerical model with conceivable implementation of the VAL-C atmosphere and a thermal pulse as an initial trigger. We find that the pulse steepens into a slow shock at higher altitudes which triggers plasma perturbations exhibiting the observed features of the surge, e.g., terminal velocity, height, width, lifetime, and heated fine structures near its base.

Export citation and abstract

BibTeX

RIS

Related links

- [NASA ADS Record](#)
- [About Related Links](#)

1. INTRODUCTION

Various types of plasma ejections in the solar atmosphere are significant in the transportation of mass and energy at diverse spatio-temporal scales (e.g., Bohlin et al. [1975](#); Innes et al. [1997](#); Shibata et al. [2007](#); Katsukawa et al. [2007](#); Culhane et al. [2007](#); Filippov et al. [2009](#); Srivastava & Murawski [2011](#); Morton et al. [2012](#), and references cited there). The magnetically structured lower solar atmosphere is dynamically filled with different types of jet-like phenomena at short spatial scales, e.g., spicules, mottles, fibrils, anemone jets, and tornadoes (e.g., De Pontieu et al. [2004](#), [2007a](#), [2011](#); Hansteen et al. [2006](#); Wedemeyer-Böhm et al. [2012](#), and references cited there). The large-scale plasma jets (such as polar jets, surges, and sprays) are also important in the channeling of mass and energy into the upper corona (e.g., Srivastava & Murawski [2011](#); Uddin et al. [2012](#), and references cited there). The magnetic reconnection and magnetohydrodynamic (MHD) wave activity are found to be the basic mechanisms for driving such plasma ejecta in the solar atmosphere (e.g., Yokoyama & Shibata [1995](#), [1996](#); Innes et al. [1997](#); De Pontieu et

al. 2004, 2007a, 2007b, 2007c; Hansteen et al. 2006; Shibata et al. 2007; Katsukawa et al. 2007; Cirtain et al. 2007; Pariat et al. 2010; Filippov et al. 2009; Murawski & Zaqrashvili 2010; Kamio et al. 2010; Murawski et al. 2011; Shen et al. 2011, 2012; Morton et al. 2012 and references cited there).

Among the various types of solar jets are the solar surges; cool jets that are typically formed by a plasma that is usually visible in H_α and other chromospheric and coronal lines (Sterling 2000). The solar surges are most likely triggered by magnetic reconnection and they exhibit different episodes of heating and cooling (Brooks et al. 2007). Solar surges are mostly associated with flaring regions and places of transient and dynamical activities in the solar atmosphere. The solar surges and their evolution at various temperatures have been observed extensively in association with magnetic field and flaring activities of the solar atmosphere (e.g., Schmieder et al. 1994; Chae et al. 1999; Yoshimura et al. 2003; Liu & Kurokawa 2004; Jiang et al. 2007; Uddin et al. 2012 and references cited there). In spite of the direct magnetic reconnection and photospheric magnetic field emergence and cancellation (Gaizauskas 1996; Sterling 2000; Liu et al. 2005; Uddin et al. 2012), solar surges can also be triggered by the impulsive generation of a pressure pulse (Shibata et al. 1982; Sterling et al. 1993), and may also be associated with explosive events (Madjarska et al. 2009). However, understanding their exact drivers requires further investigation, and more than one mechanism may trigger surge evolution depending on the local plasma and magnetic field conditions. Therefore, a study of the driving mechanisms of any particular surge is always at the forefront of solar research and may also be useful for probing the localized conditions and magnetic activities in the solar atmosphere.

In the present paper, we describe empirical results derived from the observations of a surge that originated in the western boundary of an active region NOAA AR11271 on 2011 August 25. We study the kinematics and plasma properties of this surge, as well as its most likely trigger mechanism. We select a distinct surge that was not related to the recurrent surge activities in AR11271 and apply a numerical model that reproduces its observed properties. Our model suggests that the trigger of the observed surge may be the reconnection-generated thermal pulse in the lower solar atmosphere. In Section 2 we describe the observations of the surge, its kinematics, and its derived plasma properties. We also investigate the magnetic fields at the base

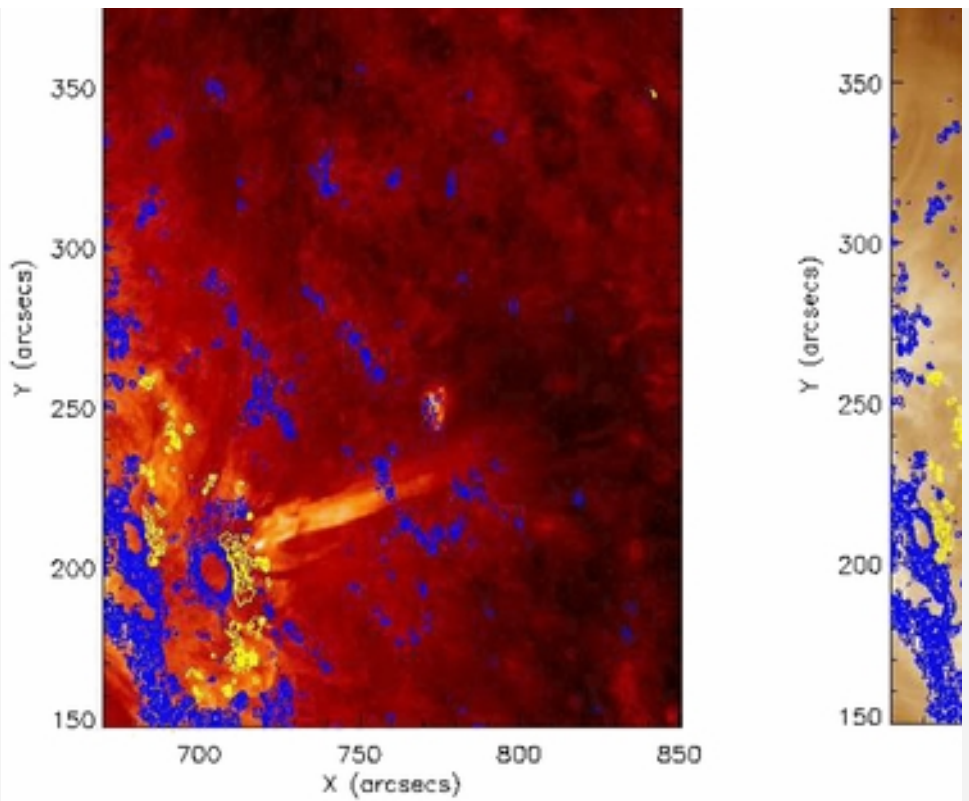
of the surge using Helioseismic Magnetic Imager (HMI) data and discuss their effects. We report on the numerical model of the observed surge and present numerical results in Section 3 and we conclude with a discussion.

2. THE KINEMATICS, PLASMA, AND MAGNETIC PROPERTIES OF A SOLAR SURGE TRIGGERED FROM AR11271

For this study we have used the imaging and magnetic field observations from instruments onboard the *Solar Dynamics Observatory (SDO)*. The Atmospheric Imaging Assembly (AIA) is a multi-channel full-disk imager (Lemen et al. 2012) with resolution elements of $0''.6$ and a cadence of 12 s. For this study we have used data of 171 \AA , 193 \AA (coronal) and 304 \AA (upper chromospheric/transition region (TR)) filters. The Helioseismic and Magnetic Imager (HMI) is designed to study the photospheric magnetic field and takes full-disk images at a cadence of 3.75 s to provide the Doppler intensity, magnetic field, and full vector magnetic field at a cadence of 45 s (Schou et al. 2012). *SDO/AIA* and *SDO/HMI* data have been obtained from the Solar-Soft cut-out service established at Lockheed Martin Space Research Laboratory, USA,³ which are corrected for flat-field and spikes. For further cleaning and calibration of this data, we also run the `aia_prep` subroutine of SSWIDL.

We use an image sequence of a solar surge in AR11271 on 2011 August 25 during 09:11–09:31 UT as observed in the 304 \AA and 193 \AA filters, which represent 10^5 K and 10^6 K plasma, respectively. The surge originated near the western boundary of AR11271 as shown in Figure 1. These images are overlaid by *SDO/HMI* magnetic field contours at a level of ± 800 G: yellow (blue) indicates positive (negative) polarity. It is clearly evident that the surge occurred near a positive polarity region (yellow) in the northwest side of a big negative polarity spot (shown by blue circle). The surge plasma mostly emits in the 304 \AA filter sensitive to the plasma temperature around $\sim 10^5$ K, but does not show much emission in the coronal filter. However, some emission in the hotter coronal channel is visible up to a height of 20–30 Mm from the foot point of the surge (see the right panel of Figure 1). Therefore, the surge consists of multi-temperature plasma.





[Zoom In](#) [Zoom Out](#)

[Reset image size](#)

Figure 1. *SDO/AIA* 193 \AA (right, yellow-brown map for 1.0 MK plasma) and 304 \AA (left, red temperature map for 0.1 MK plasma) EUV images overlaid by HMI magnetic field contours of maximum level ± 800 G. Yellow (blue) contours show positive (negative) polarity of the magnetic field. The surge origin is accompanied by heating above its foot point. The observed surge is clearly evident in the HeII 304 \AA filter that is sensitive to the low-temperature plasma of 0.1 MK. Some heated part of the surge especially near its base up to the height of 20–30 Mm is also evident in the coronal filters (e.g., 193 \AA) that are sensitive to the plasma temperature around 1.0 MK. The surge is originated from the western boundary of the positive polarity situated in the northwest direction of the big sunspot with negative polarity as represented by the blue circular contour at $X = 700''$, $Y = 200''$.

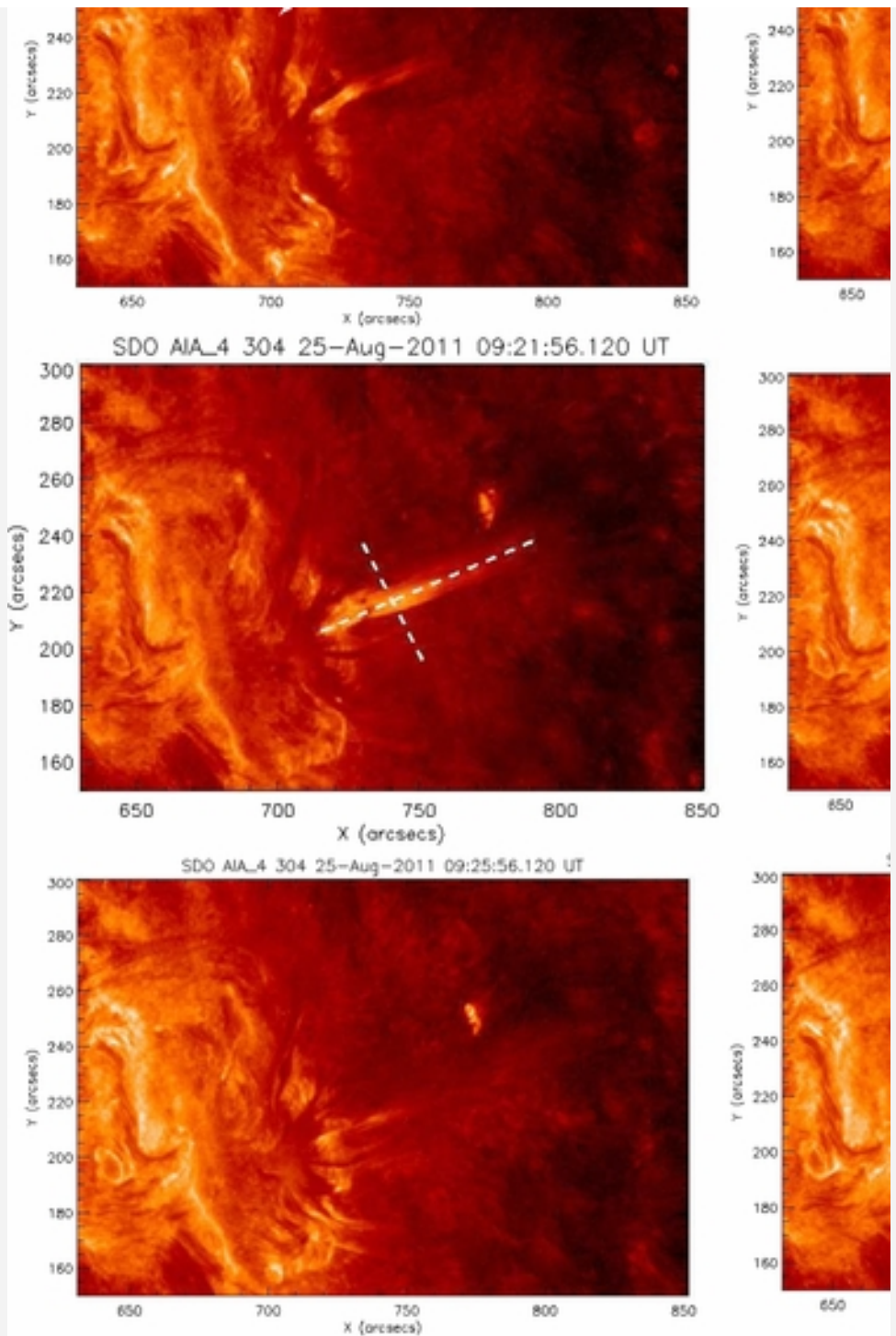
Download figure:

[Export PowerPoint slide](#)

2.1. Kinematics of the Surge

Figure 2 represents the spatio-temporal evolution of the surge material using the sub-field data. It is clear that the surge was activated at 09:11 UT near the western boundary of NOAA AR11271, and faded around 09:31 UT. The observed surge was not associated with the recurrent spray surge activity in AR11271 (P. Kayshap et al. 2013, in preparation). This image sequence shows that the surge reaches a projected height of ≈ 65 Mm in ≈ 660 s. The terminal speed of the surge is found to be ≈ 100 km s $^{-1}$. This surge is well collimated with a maximum width of ≈ 7 Mm and does not show any significant lateral expansion. Its decelerating time was ≈ 500 s in which it also gradually faded. The top panel of Figure 3 shows the distance-time measurement along the observed surge. It is evident that the denser core material of the surge first rises up and then decelerates. Some fainter and less dense plasma reaches much higher into the solar atmosphere and falls freely thereafter. The distance-time map across the surge at a particular height around ~ 15 Mm from its footpoint is shown in the bottom panel. The radiance periodicity is observed on a 3.0 minute timescale, which may be the signature of the periodic enhancement of mass density in the surge. This may provide the clues about the periodic driver of the surge, which will be discussed in detail in Section 3. It is also possible that the periodicity of 3.0 minutes near the surge base may be due to the swirling motion as recently observed in spectroscopic data (e.g., Wedemeyer-Böhm et al. 2012; De Pontieu et al. 2012 and references cited therein). However, such small-scale motion is below the detection limit in our data. Moreover, the radiance oscillations occur higher in the TR, and therefore, in the present case it may be the most likely evidence of the periodic signature of the arrival of slow shocks in the upper chromosphere/TR.



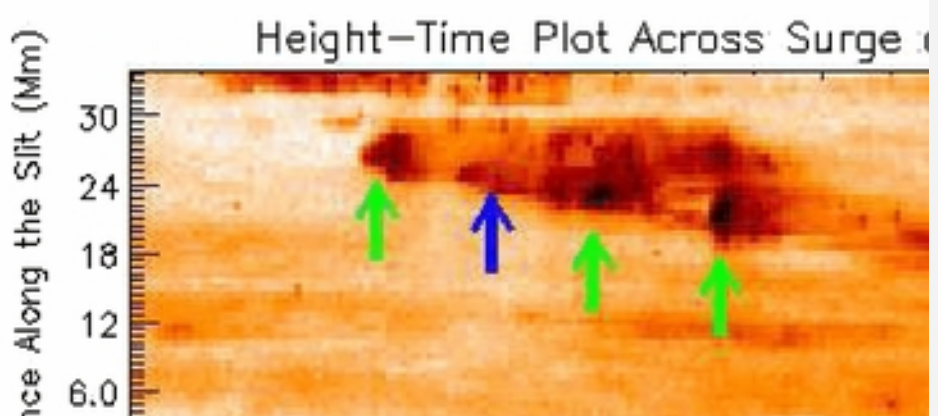
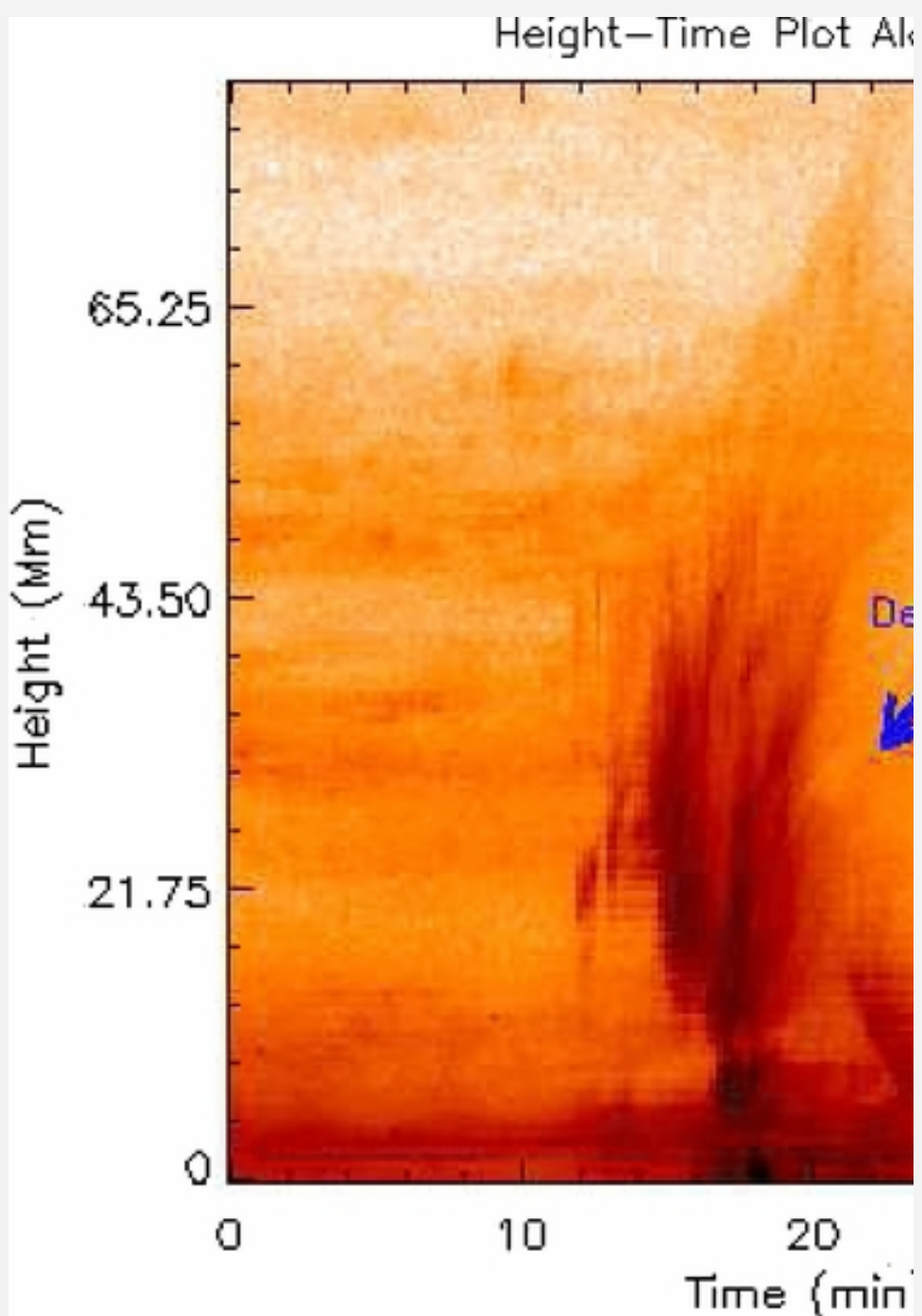


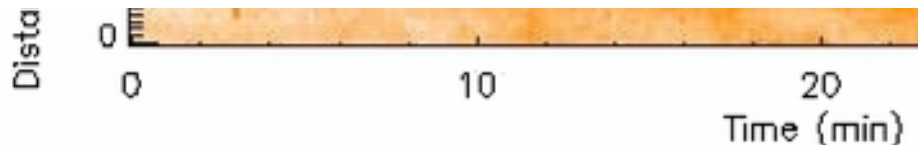
[Zoom In](#) [Zoom Out](#)

[Reset image size](#)

Figure 2. *SDO/AIA 304Å time sequence of a surge propagation higher into the corona from the boundary of an active region NOAA AR11271. The surge fades gradually with time, and the material tries to settle down due to gravity. Horizontal and vertical dotted lines on the snapshot of 09:21 UT show the two paths along which the distance–time measurements have been made.*

[Download figure:](#)

[Standard image](#)[High-resolution image](#)[Export PowerPoint slide](#)



[Zoom In](#) [Zoom Out](#)

[Reset image size](#)

Figure 3. Height–time plots: along the solar surge using He β ii 304Å data (top) where the distance is measured along the slit chosen along the surge; across the surge at a height of \approx 15 Mm from its footpoint (bottom) where the distance is measured along the slit chosen across the surge. The approximate positions of both slits are shown over the 09:21 304Å snapshot in Figure 2.

Download figure:

[Standard image](#)

[High-resolution image](#)

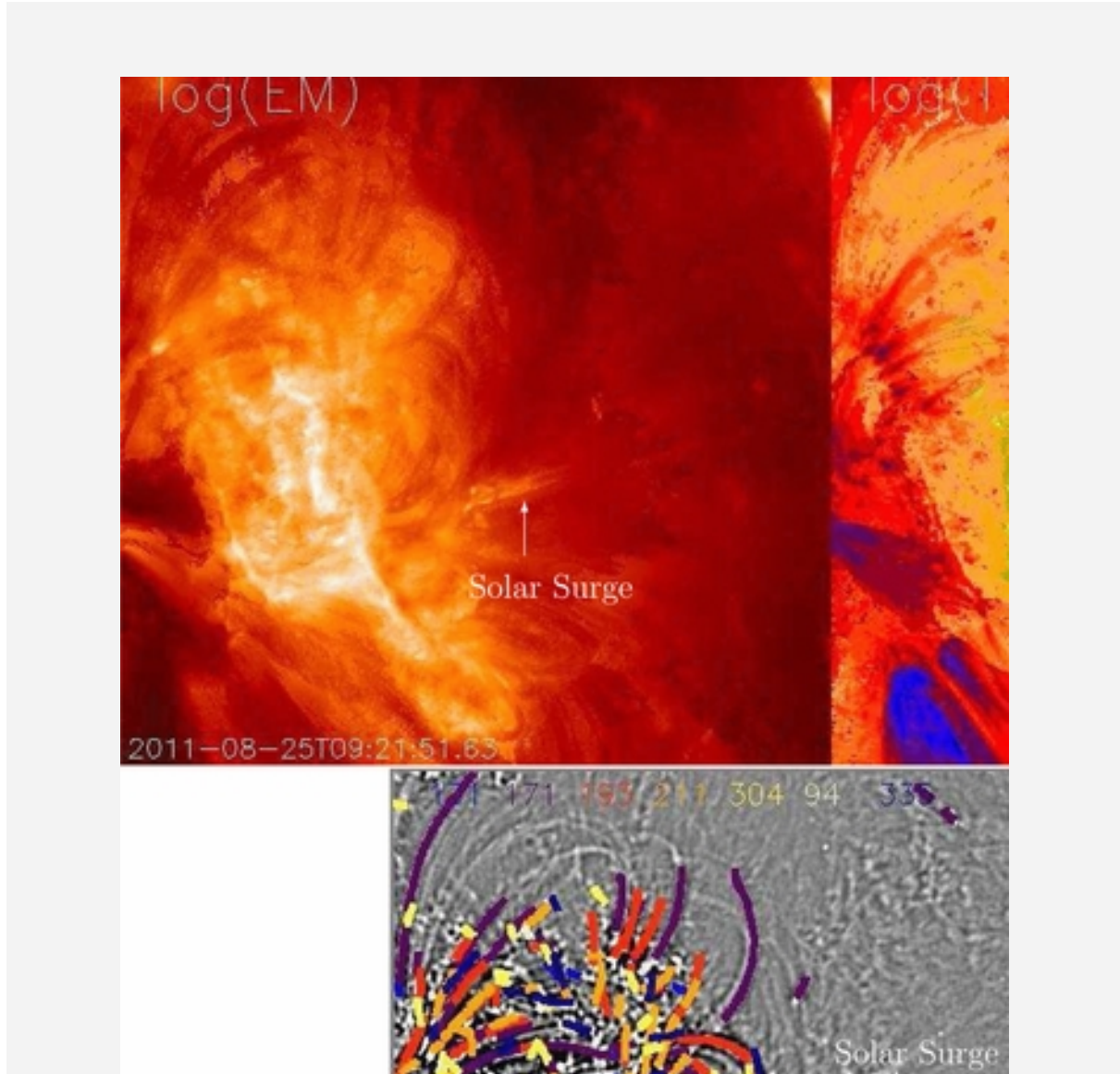
[Export PowerPoint slide](#)

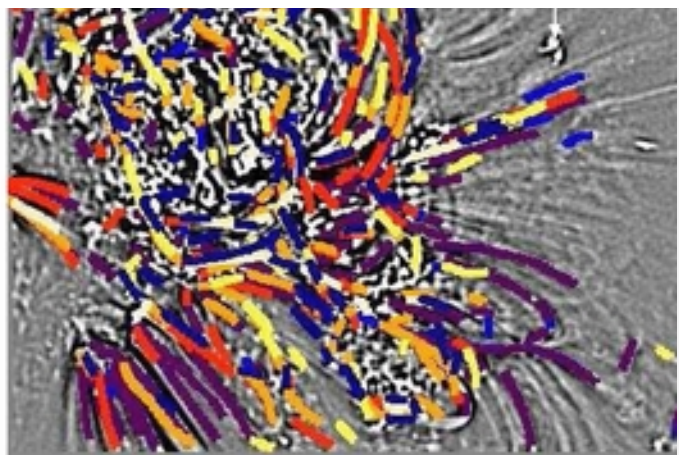
2.2. Estimations of the Average Temperature and Density of the Surge

In this section, we carried out emission measure and temperature distribution analysis as well as tracing and estimating the density along the surge by extensively using the automated method developed by Aschwanden et al. (2011). Understanding such plasma properties provides more clues about the driver of the surge, while comparing with the numerical results. *SDO/AIA* data provide information about the emission measure and estimation of the average density and temperature (Aschwanden et al. 2011). We use the full-disk *SDO/AIA* in all EUV channels at the time of the maximum rise of the surge around 09:22 UT on 2011 August 25. We calibrate and clean the data using the `aia_prep` subroutine of SSWIDL and co-align the AIA images as observed in various AIA filters by using the co-alignment test as described by Aschwanden et al. (2011).

Using the automated code developed by Aschwanden et al. (2011), we obtain

emission measure and temperature maps for six AIA filter full-disk and co-aligned images (304 \AA , 171 \AA , 193 \AA , 94 \AA , 335 \AA , and 211 \AA) in the temperature between 0.5–9.0 MK. The emission measure map in the top left panel of Figure 4 shows that the surge has significant emissions from its denser core. The emission from its leading edge is comparatively low. The top right panel of Figure 4 shows the distribution of temperature in and around the surge location. It is evident that heating is confined near its foot point. Greenish-yellow regions represent the highest temperature in and around the foot point of the surge. The reddish region shows the plasma at the base of the surge with a temperature of 6.2–6.3 MK. Above the heated area near the base of the surge, the cool plasma is maintained at sub-coronal temperatures as represented by blue–black colors. It is also mixed with the comparatively hot plasma. The leading edge of the surge is, however, maintained at comparatively high coronal temperatures. The heating near the base of the surge probably drives it, and the cool plasma moves behind the hot plasma at its leading edge. It is also mixed with the hot plasma and constitutes the multi-temperature surge.





[Zoom In](#) [Zoom Out](#)

[Reset image size](#)

Figure 4. Emission measure (EM) map (top left) and temperature map (top right panel): evidence of the multi-temperature plasma forming the surge. The lower part of the surge consists of cool plasma, while the leading edge exhibits coronal temperatures. The bottom panel shows the automated tracing of the plasma threads as visible at various temperatures along the open field lines of the surge as shown by the arrow using the methodology of Aschwanden et al. (2011). Color codes for the emitting plasma in different AIA channels are shown at the top of this snapshot.

Download figure:

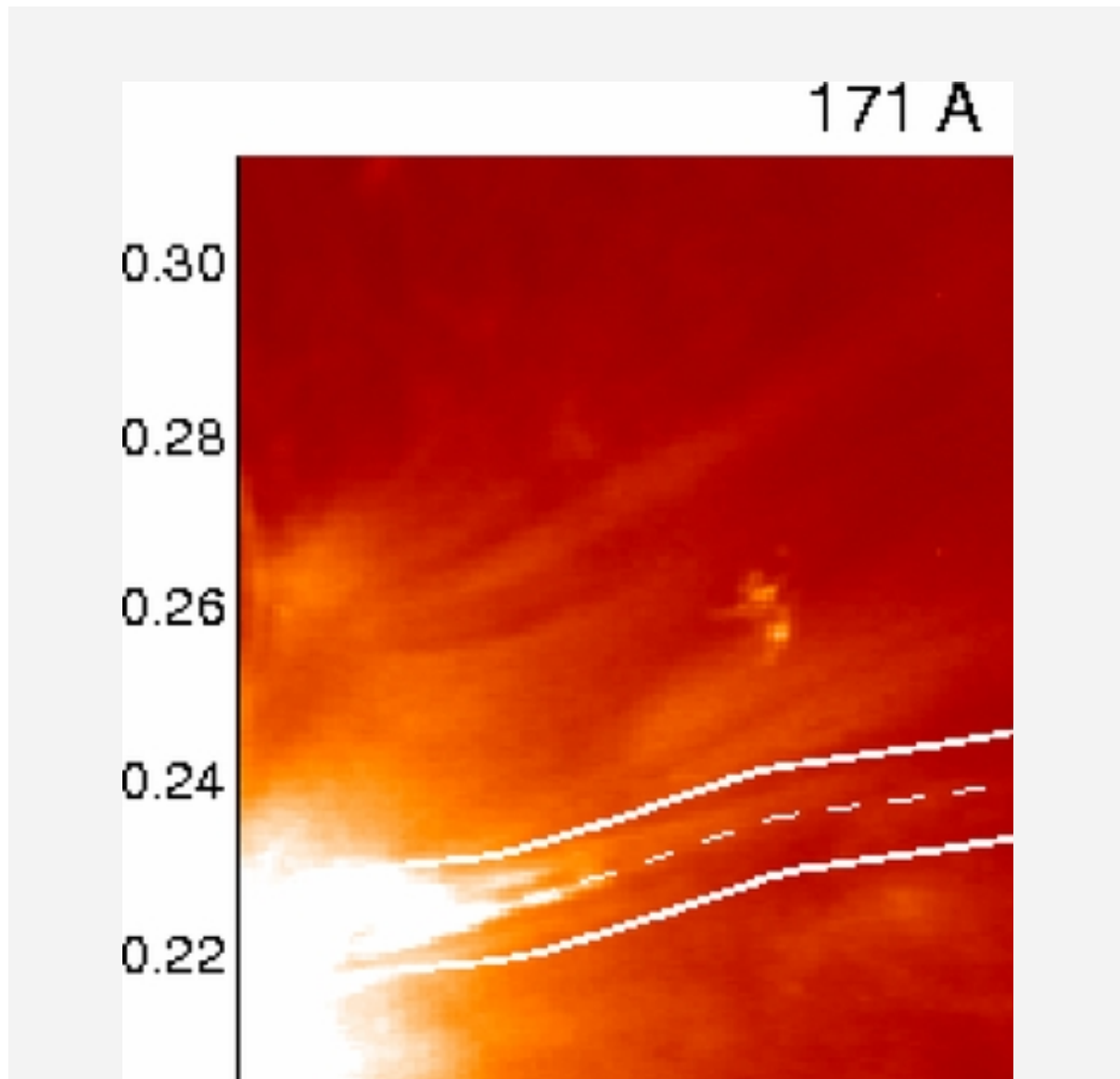
[Standard image](#)

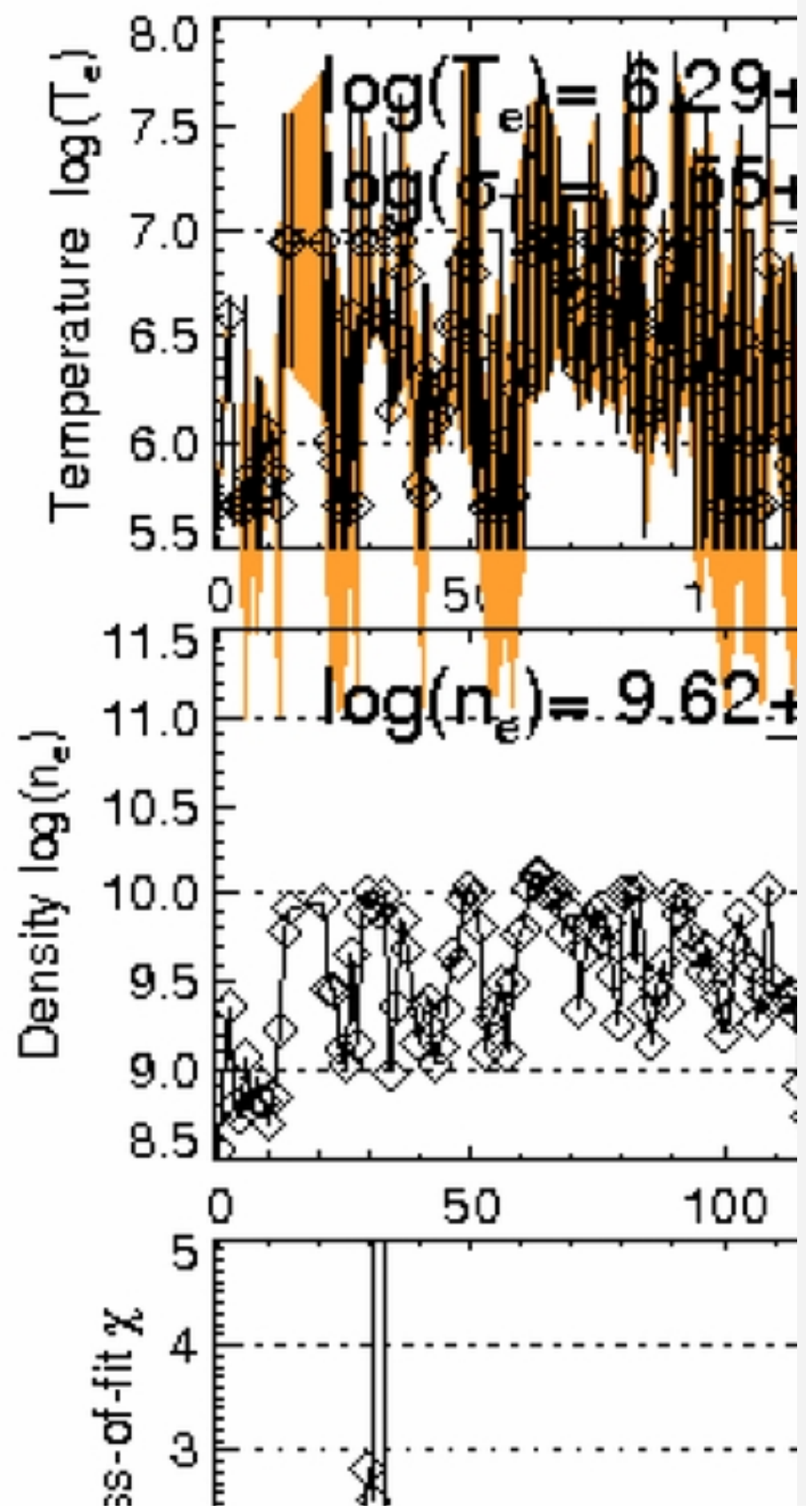
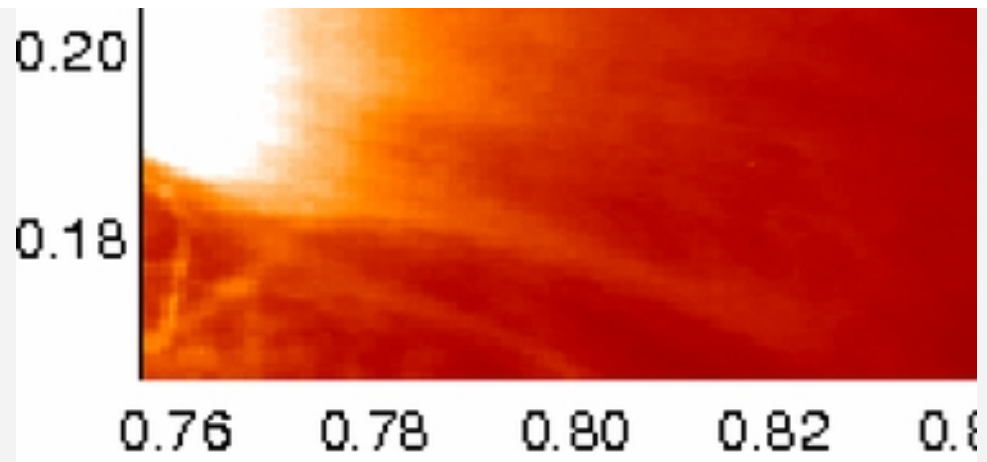
[High-resolution image](#)

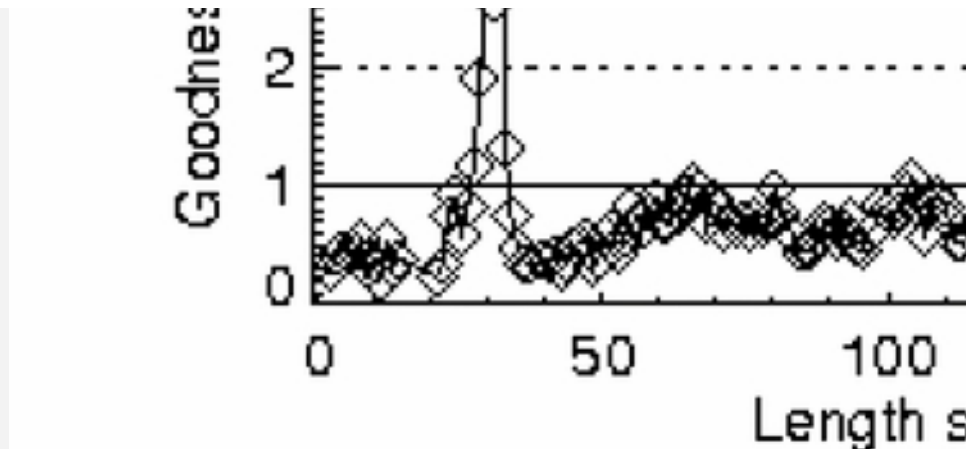
[Export PowerPoint slide](#)

Using the automated procedure (Aschwanden et al. 2011), we trace the loop segments and surge in the co-spatial and co-temporal images of various wavelengths of *SDO/AIA* data. The input free parameters for this automated tracing of the surge are summarized in Table 1. The bottom panel of Figure 4 shows that the surge material is erupting along open field lines, indicated by the white arrow, from the western part of the active region boundary. The surge consists of multi-

temperature plasma. The contribution of cool surge plasma ($T= 0.1$ MK) as evident in the 304\AA channel is represented by yellow color. For the estimation of the plasma properties (temperature and density) along the surge material and its overlying diffuse corona, we trace the larger segment of this coronal structure using another set of free parameters (cf. Table 1) and implement the best forward fit of the possible differential emission measure (DEM) solutions. We choose this set of free parameters on the basis of trial and error, and it gives the best DEM forward fit in the case of 171\AA fluxes at each pixel of the considered region around the surge and its overlying atmosphere. In Figure 5, the estimated density and temperature are displayed. The chi-square of the estimation in the forward modeling is good enough up to 70 Mm along the surge as well as up to ~ 130 Mm in its overlying diffuse corona. The average temperature and density of the surge material are, respectively, 2.0 MK and $4.1 \times 10^9 \text{ cm}^{-3}$. We can estimate these physical parameters in all the traced structures in all AIA channels. However, we display the best-fit results of the estimation of the density and temperature along the surge and its overlying corona in the 171 \AA channel as shown in Figure 5.







[Zoom In](#) [Zoom Out](#)

[Reset image size](#)

Figure 5. AIA 171Å image (top panel) displays the sub-field containing the surge and its overlying diffuse corona. The image axes are scaled as a fraction of the solar radius. This panel shows the 171Å image in which the box shows the area along the surge and its overlying diffuse corona along which the physical parameters are evaluated. The estimated plasma properties, e.g., the integrated density, and temperature along the surge (dashed line) during its maximum rise, are displayed in two consecutive middle panels.

Download figure:

[Standard image](#)

[High-resolution image](#)

[Export PowerPoint slide](#)

Table 1. Summary of Input Free Parameters

	Half Width	Threshold Level in Standard Flux Deviation	Min Filling Factor	Output Resolution	Minimum Length	Max Traced Curvature Structures	Min Radius
To trace the surge	2 pixels	1.0	0.35	5.0	0.01	10,000	25
To estimate the plasma properties	10 pixels	1.0	0.15	5.0	0.04	10,000	60

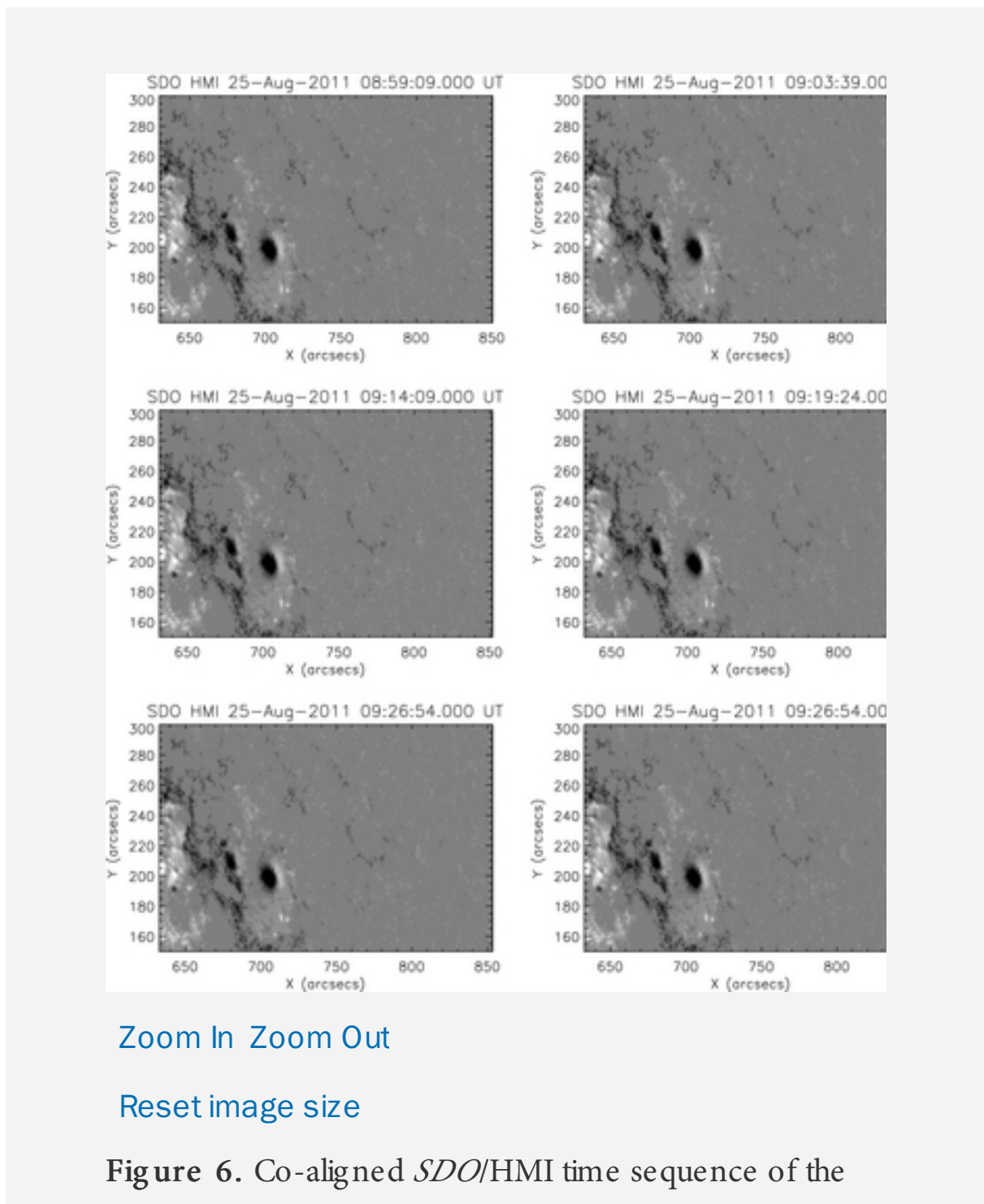
Download table as:

[ASCII](#)[Typeset image](#)

2.3. **SDO/HMI Investigations of the Magnetic Field Properties at the Base of the Surge**

The surge occurred at the northwestern side of the big sunspot with negative polarity. It was located at the outer layer of a positive polarity region (cf. snapshot on 09:00 UT in Figure 6). The surge is shown as an intensity contour (blue) of co-aligned AIA data on the HMI snapshot of 09:21 UT in Figure 6. The morphology of the origin site of the observed surge is almost similar to that observed recently by Uddin et al. (2012) in association with the recurrent surges from NOAA 10884 on 2003 October 25. However, we do not observe any strong signature of the magnetic field annihilation as well as moving magnetic features (MMFs) in our present observational data as previously observed by Uddin et al. (2012). Therefore, we infer that the observed surge may not be triggered by strong photospheric magnetic field activities. It is evident that tiny negative magnetic polarities have evolved near the surge location and the major positive polarity region has shown some aerial enhancement toward the western direction. Therefore, such rearrangements of the magnetic polarities around the surge region may produce more complexity in the overlying magnetic flux tubes (Roy 1973; Canfield et al. 1996), e.g., in low-lying loops and an arch crossing near the base of the surge (cf.

09:11 UT AIA 304Å snapshot of Figure 2; HMI-AIA snapshot on 09:20 UT in Figure 6). Therefore, the chromospheric reconnection between the open field lines and surrounding closed fields may trigger the surge. The localized brightening and heating at the same location is evident where dark arch-type flux tube and low-lying closed loops are crossing near the surge base (cf. 09:11 UT snapshot of Figure 2 and the right panel of Figure 4), which may generate the thermal pulse probably triggering the observed plasma perturbations. In the next section, in support of the present observational baseline of the triggering of the surge due to chromospheric heating, we devise a numerical model with implementation of the VAL-C atmosphere and a thermal pulse as an initial trigger, which reproduces the observations closely.



photospheric magnetic field near the origin of the surge.

The blue surge is shown as an intensity contour on the HMI snapshot of 09:21 UT. The blue loop arches on both sides of the surge may cause possible reconnection at its base to heat and subsequently launch a thermal pulse for its acceleration.

Download figure:

[Standard image](#)

[High-resolution image](#)

[Export PowerPoint slide](#)

3. A NUMERICAL MODEL FOR THE PULSE-DRIVEN SOLAR SURGE

To reproduce the observed surge, our model system assumes a gravitationally stratified solar atmosphere that is described by the ideal two-dimensional (2D) MHD equations:

$$\frac{\partial \varrho}{\partial t} + \nabla \cdot (\varrho \mathbf{V}) = 0, \quad (1)$$

$$\varrho \frac{\partial \mathbf{V}}{\partial t} + \varrho (\mathbf{V} \cdot \nabla) \mathbf{V} = -\nabla p + \frac{1}{\mu} (\nabla \times \mathbf{B}) \times \mathbf{B} + \varrho \mathbf{g}, \quad (2)$$

$$\frac{\partial p}{\partial t} + \nabla \cdot (p \mathbf{V}) = (1 - \gamma) p \nabla \cdot \mathbf{V}, \quad (3)$$

$$\frac{\partial \mathbf{B}}{\partial t} = \nabla \times (\mathbf{V} \times \mathbf{B}), \quad \nabla \cdot \mathbf{B} = 0. \quad (4)$$

Here ϱ , \mathbf{V} , \mathbf{B} , $p = (k_B/m)\varrho T$, T , $\gamma = 5/3$, $\mathbf{g} = (0, -g)$ with its value $g = 274 \text{ m s}^{-2}$, m , k_B , are, respectively, the mass density, flow velocity, magnetic field, gas pressure, temperature, adiabatic index, gravitational acceleration, mean particle mass, and Boltzmann's constant. It should be noted that we do not invoke the radiative cooling and thermal conduction in our model for simplicity reasons since we simulate the cool surge ejecta in the solar atmosphere.

3.1. Equilibrium Configuration

We assume that at its equilibrium the solar atmosphere is still ($\mathbf{V}_e = \mathbf{0}$) with a force-free magnetic field,

$$(\nabla \times \mathbf{B}_e) \times \mathbf{B}_e = \mathbf{0}, \quad (5)$$

such that it satisfies a current-free condition, $\nabla \times \mathbf{B}_e = \mathbf{0}$, and it is specified by the magnetic flux function, A , as

$$\mathbf{B}_e = \nabla \times (A \hat{\mathbf{z}}). \quad (6)$$

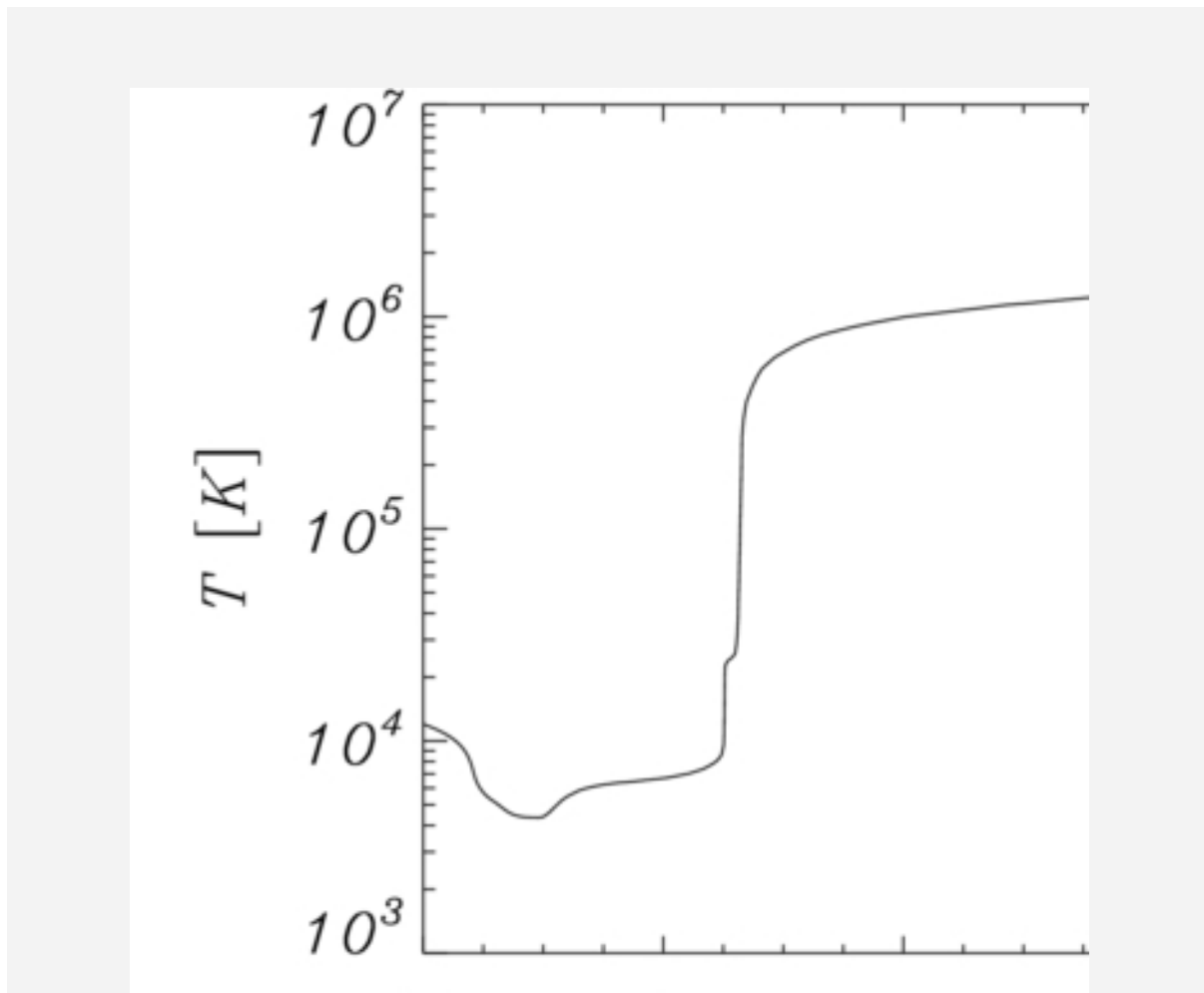
Here the subscript "e" corresponds to equilibrium quantities. We set an arcade magnetic field by choosing

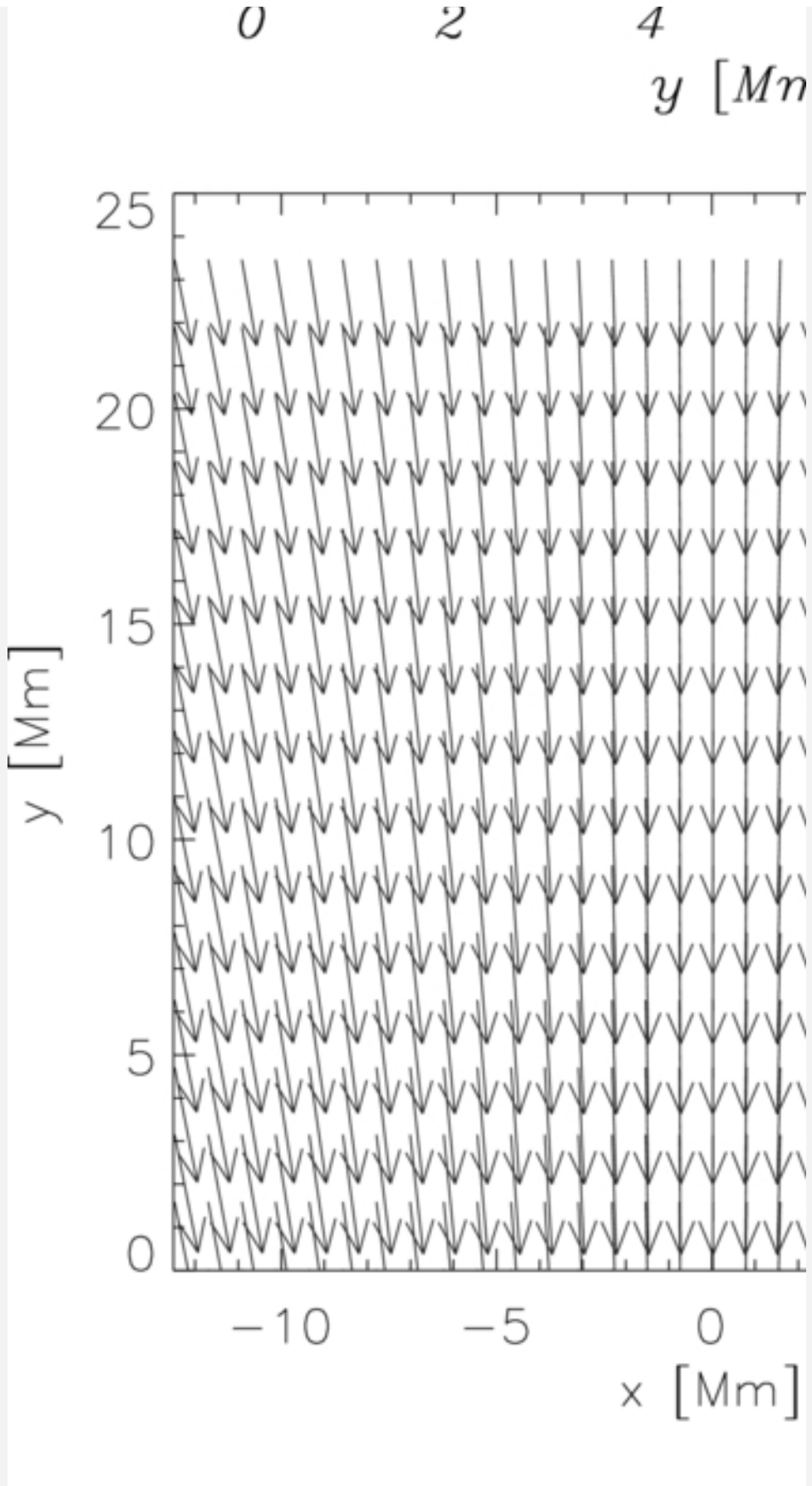
$$A(x, y) = B_0 \Lambda_B \cos(x/\Lambda_B) \exp[-(y - y_r)/\Lambda_B] \quad (7)$$

with B_0 being the magnetic field at $y = y_r$ and the magnetic scale-height is

$$\Lambda_B = \frac{2L}{\pi}. \quad (8)$$

We set and hold fixed $L = 100$ Mm. For such a choice the magnetic field vectors are weakly curved (Figure 2, bottom panel).





[Zoom In](#) [Zoom Out](#)

[Reset image size](#)

Figure 7. Equilibrium profile of solar temperature (top panel) and magnetic field vectors (bottom panel). The magnetic field is expressed in units of 44 G and a part of the simulation region is displayed.

Download figure:

Standard image

High-resolution image

Export PowerPoint slide

As a result of Equation (5) the pressure gradient is balanced by the gravity force,

$$-\nabla p_e + \varrho_e \mathbf{g} = \mathbf{0}. \quad (9)$$

With the ideal gas law and the y -component of Equation (9), we arrive at

$$p_e(y) = p_0 \exp \left[- \int_{y_r}^y \frac{dy'}{\Lambda(y')} \right], \quad \varrho_e(y) = \frac{p_e(y)}{g \Lambda(y)}, \quad (10)$$

where

$$\Lambda(y) = \frac{k_B T_e(y)}{mg} \quad (11)$$

is the pressure scale height, and p_0 denotes the gas pressure at the reference level that we choose in the solar corona at $y_r = 10$ Mm.

We take an equilibrium temperature profile $T_e(y)$ for the solar atmosphere derived from the VAL-C atmospheric model of Vernazza et al. (1981). Having specified $T_e(y)$ (see Figure 2, top panel) with Equation (10) we obtain the corresponding gas pressure and mass density profiles.

The TR is located at $y \approx 2.7$ Mm. Above the TR we assume an extended solar corona. Below the solar chromosphere, the temperature minimum is located at $y \approx 0.9$ Mm.

3.2. Perturbations

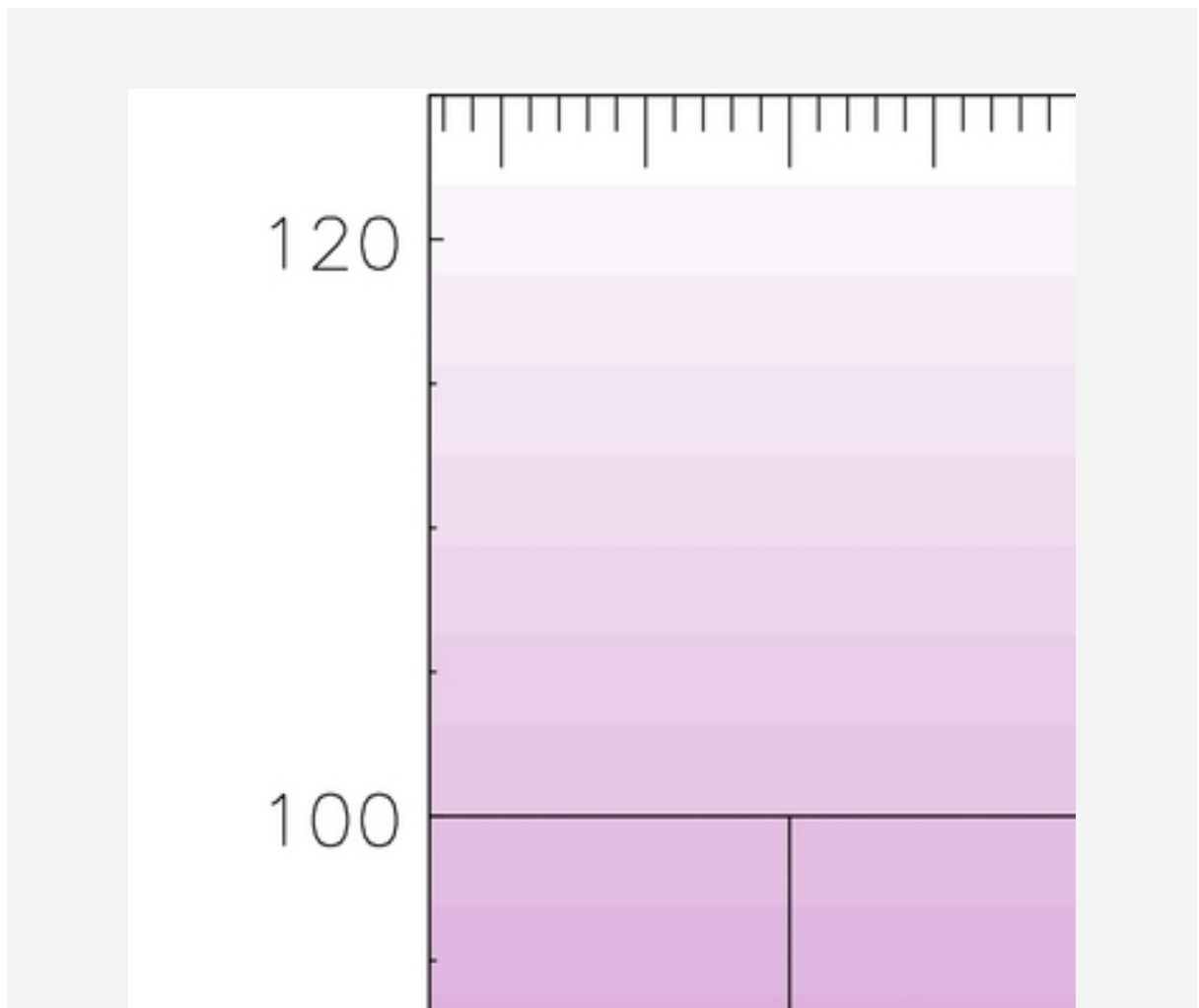
We initially perturb the equilibrium impulsively by a Gaussian pulse in a gas pressure, viz.,

$$p(x, y, t = 0) = p_e(y) + p_e(y)A_p \times \exp \left[-\frac{(x - x_0)^2}{w_x^2} - \frac{(y - y_0)^2}{w_y^2} \right]. \quad (12)$$

Here A_p is the amplitude of the pulse, (x_0, y_0) is its initial position, and w_x, w_y denote its widths along the x - and y -directions, respectively. We set and hold fixed $A_p = 80$, $x_0 = 0$ Mm, $y_0 = 1.75$ Mm, $w_x = 2.25$ Mm, and $w_y = 0.2$ Mm.

3.3. Results of the Numerical Simulations

Equations (1)–(4) are solved numerically using the FLASH code (Lee & Deane [2009](#); Fryxell et al. [2000](#)). This code uses a second-order unsplit Godunov solver with various slope limiters and Riemann solvers, as well as adaptive mesh refinement (AMR). We set the simulation box of $(-12.5, 12.5) \times (0, 125)$ Mm² along the x - and y -directions (Figure 8, bottom panel) and set and hold fixed all plasma quantities at all boundaries of the simulation region to their equilibrium values which are given by Equations (6) and (10). These fixed boundary conditions performed much better than transparent boundaries, leading only to negligibly small numerical reflections of wave signals from these boundaries.



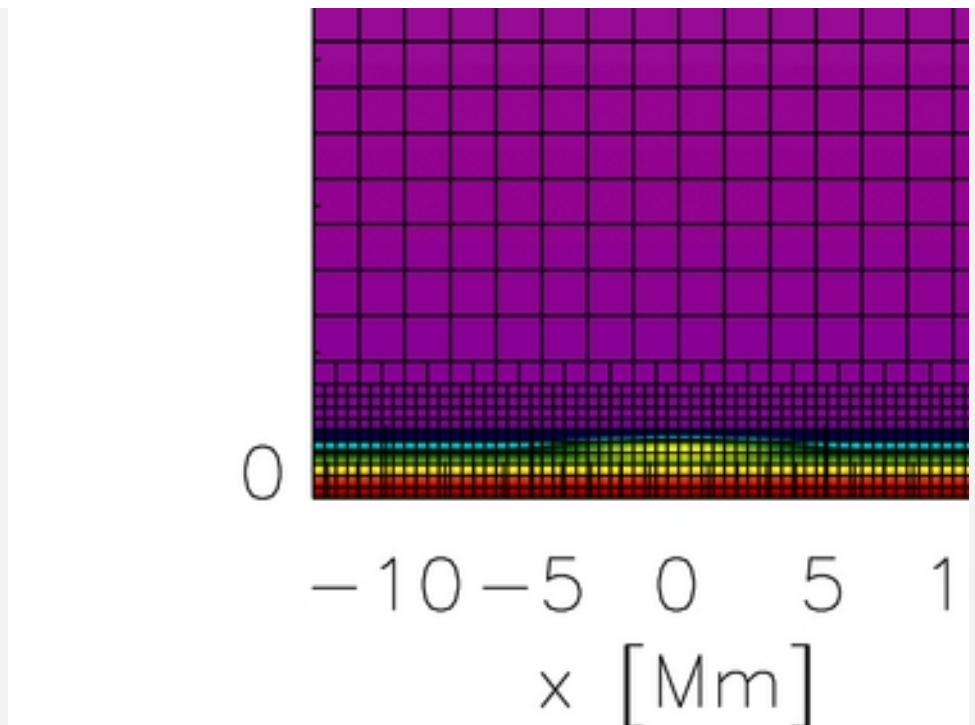
y [Mm]

80

60

40

20



[Zoom In](#) [Zoom Out](#)

[Reset image size](#)

Figure 8. Grid system with block boundaries represented by solid lines as adopted in the simulation. The initial pressure perturbation of the system is displayed by the horizontally elongated patch at a location (0 Mm, 1.75 Mm).

Download figure:

[Standard image](#)

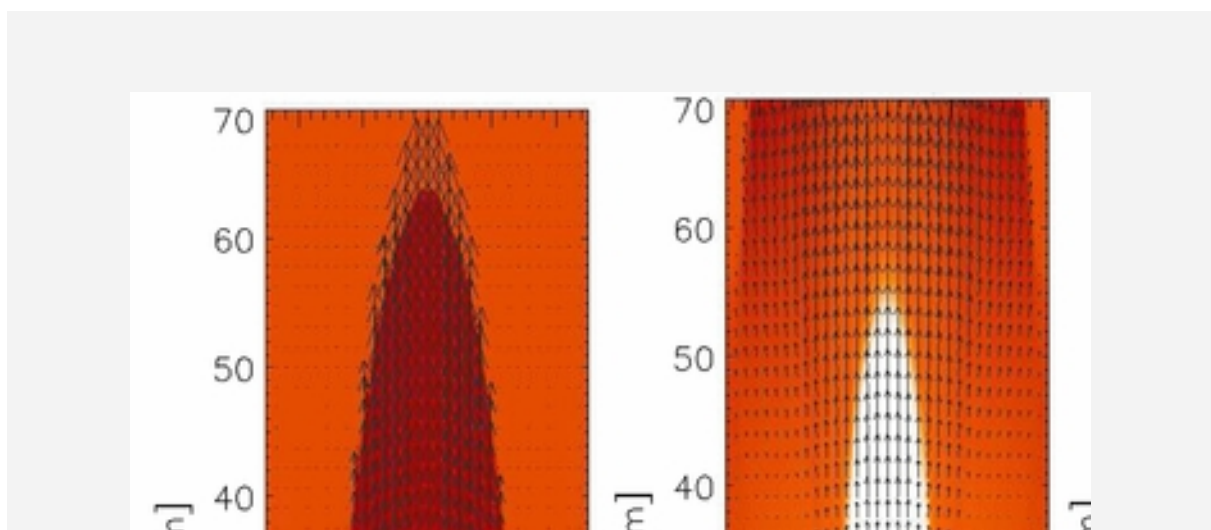
[High-resolution image](#)

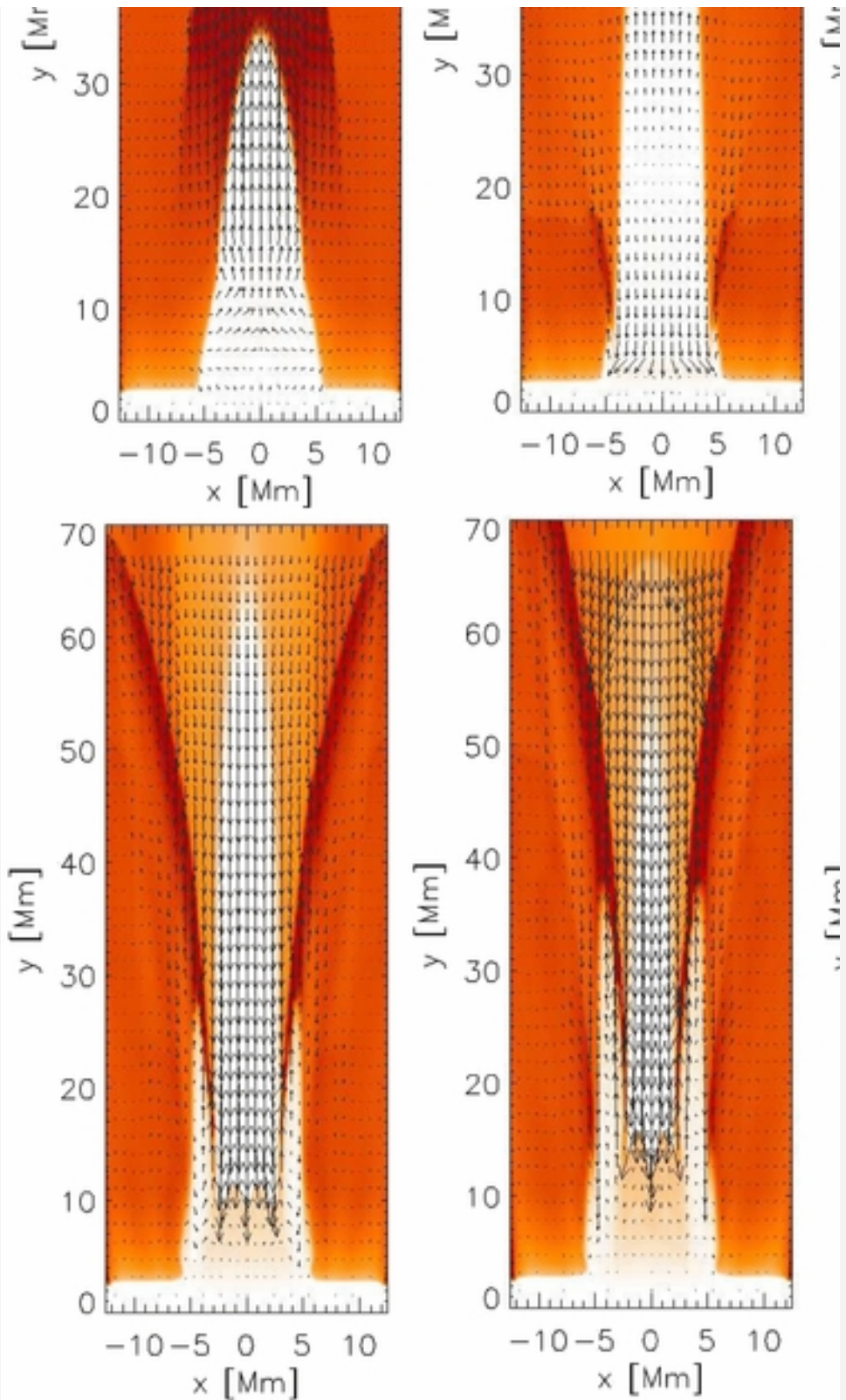
[Export PowerPoint slide](#)

In our modeling, we use an AMR grid with a minimum (maximum) level of refinement set to 4 (7) (Figure 8). The refinement strategy is based on controlling numerical errors in mass density, which results in an excellent resolution of steep spatial profiles and greatly reduces numerical diffusion at these locations.

Figure 9 displays the spatial profiles of the plasma temperature (color maps) and velocity (arrows) resulting from the initial pulse of Equation (12), which splits into counter-propagating pulse trains. The downward-propagating part reflects the dense

ambient plasma of the photosphere. This reflected part lags behind the originally upward-propagating pulses, which become slow shocks. Because the plasma is initially pushed upward, the under-pressure results in the region below the initial pulse. This under-pressure sucks up comparatively cold chromospheric plasma, which lags behind the shock front at higher temperature. As a result, the pressure gradient force works against gravity and forces the chromospheric material to arrive into the solar corona in the form of a rarefaction wave. At $t = 200$ s this shock reaches the altitude of $\gamma \approx 65$ Mm and the cold plasma edge is located at $\gamma \approx 35$ Mm, which is below the slow shock. The reason for the material being lifted up is the rarefaction of the plasma behind the shock front, which leads to low pressure there. The next snapshot (top middle panel) is drawn for $t = 400$ s. At this time the chromospheric plasma is located below at $\gamma \approx 55$ Mm. At the next moment, $t = 600$ s (top right panel), the chromospheric plasma shows its developed phase, reaching the level of $\gamma = 65$ Mm, which approximately matches the observational data of Figure 2 (top right panel). The cool surge slows down while propagating upward. At $t = 800$ s it arrives at the level of $\gamma \approx 70$ Mm and subsequently subsides because it is attracted by gravity (bottom panels). At the subsiding stage the heated fine structures develop as a result of interaction between the down-falling plasma. During the evolution of the surge, the comparatively hot plasma is evident near the base of the simulated surge that qualitatively matches the observations. The leading front of the slow shock moving above the cool surge plasma may also leave some traces in the overlying diffused quiet-Sun atmosphere evident in the coronal filters (see the right panel of Figure 1). However, the less dense and diffused overlying quiet-Sun may not be visible as a tracer of a slow shock front. The temporal evolution of the density reveals that the surge is denser near its base, while the density decreases with height (Figure 10). This is consistent with the observational data.





Reset image size

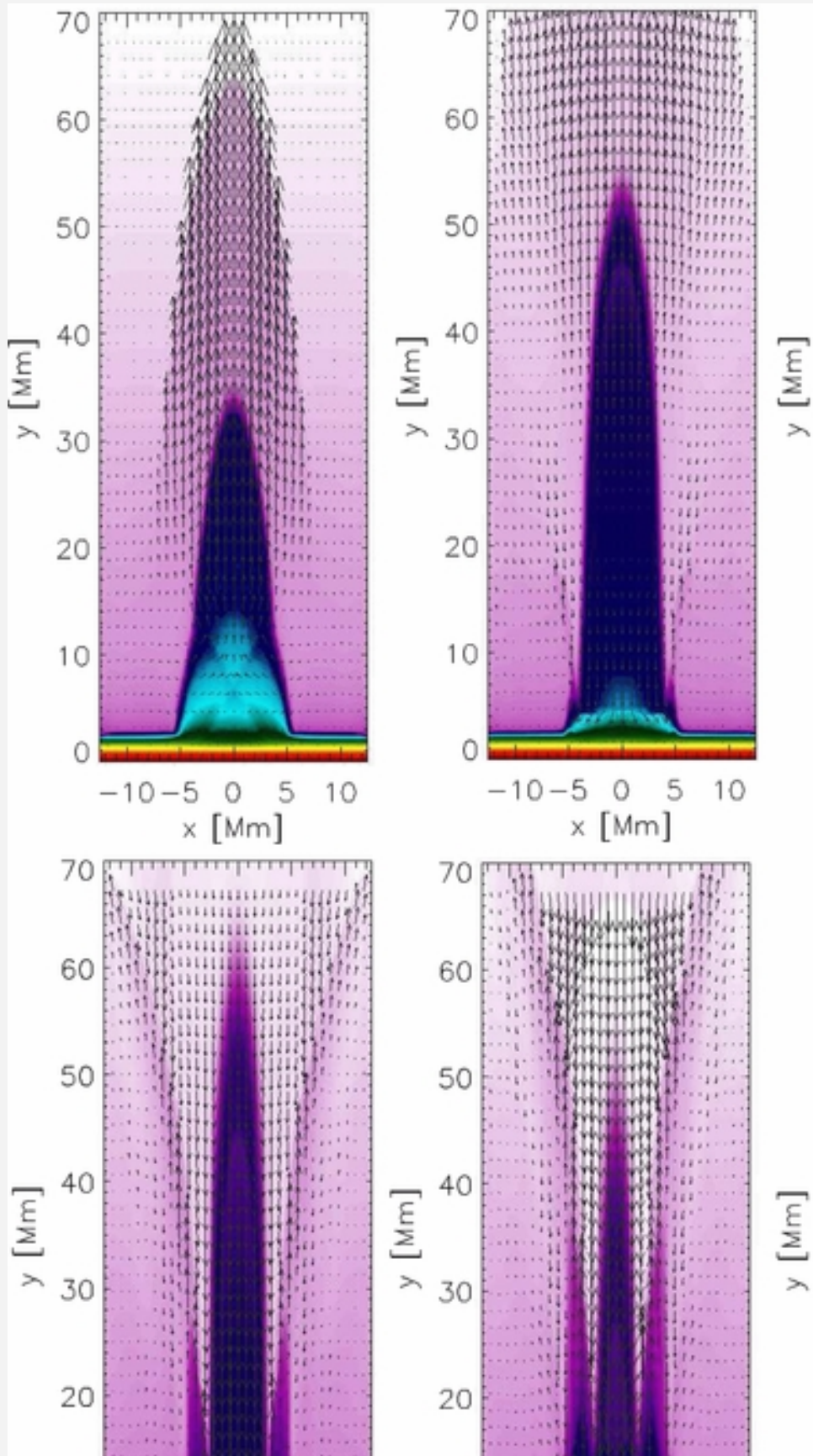
Figure 9. Temporal snapshots of a simulated surge. The temperature (color maps) profiles at $t = 200$ s, $t = 400$ s, $t = 600$ s, $t = 800$ s, $t = 1000$ s, and $t = 1200$ s (from top to bottom). Temperature is drawn in units of 1 MK as shown in the color bar, which is common to all the panels. The velocity vector unit is 150 km s^{-1} .

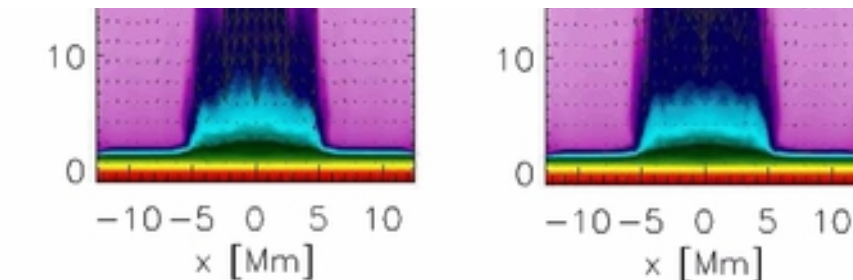
Download figure:

[Standard image](#)

[High-resolution image](#)

[Export PowerPoint slide](#)





[Zoom In](#) [Zoom Out](#)

[Reset image size](#)

Figure 10. Temporal snapshots of a simulated surge.

The density (color maps) profiles at $t = 200$ s, $t = 400$ s, $t = 600$ s, $t = 800$ s, $t = 1000$ s, and $t = 1200$ s (from top to bottom). Density is drawn in the units of 10^{-12} kg m $^{-3}$ as shown in the color bar, which is common to all the panels. The velocity vector unit is 150 km s $^{-1}$.

Download figure:

[Standard image](#)

[High-resolution image](#)

[Export PowerPoint slide](#)

4. DISCUSSION AND CONCLUSION

In the present paper, we studied the kinematics and plasma properties of the solar surge triggered in AR11271 on 2011 August 25. We also performed a 2D numerical simulation using the VAL-C model of the solar atmosphere as an initial condition and the FLASH code (Fryxell et al. 2000), which approximately reproduce the dynamics of the observed cool surge. The surge rises vertically from its origin site up to a height of ≈ 65 Mm with a terminal velocity of ≈ 100 km s $^{-1}$, and thereafter falls and fades gradually within its total lifetime of ≈ 20 minutes. We also measure the temperature and density distribution of the observed surge during its maximum rise, and its average temperature and density are, respectively, 2.0 MK and 4.1×10^9 cm $^{-3}$. We do not get any strong evidence of the photospheric magnetic field activity (i.e., MMFs, flux-emergence, field annihilation, etc.) in support of the formation of the observed surge. The surge is most likely found to be driven by

magnetic reconnection-generated thermal energy in the chromosphere.

The numerical simulations exhibit a general scenario of rising and subsequently down falling/fading of the observed surge with a number of observational features such as its height and width, ejection, approximate rising timescale, and average rising velocity which are close to the observational data. The heated fine structures at the base of the surge also in both the observations and theory match well. The temperature distribution (Figure 4) shows that the significant amount of cool plasma expands along the surge, while its leading edge is maintained at coronal temperatures. This scenario matches qualitatively with our simulation results when the comparatively cooler core plasma of a surge lags behind the high-temperature slow shock. The kinematical estimations of the surge (Figure 3) also reveal the acceleration of the surge material and its subsequent free fall due to gravity thereafter, which also matches the simulation results well. However, some parts of the comparison between the numerical and observational data are approximate and only qualitative. This mismatch may result from simplified profiles of the parameters in our numerical model. Moreover, the real surge was excited in more complex plasma and magnetic field conditions at the boundary of AR11271.

It is reported in the literature that if the height of the energy release site is less (greater) than a critical height then the jet will be driven by crest shocks (directly by the pressure gradient force generated by an explosion; Shibata et al. 1982). However, this minimum critical height in the solar atmosphere depends on the strength of the pressure enhancement with time at the energy release site. For larger pressure enhancement, this height will be lower and vice versa. Under conditions when the energy release site is higher in the solar atmosphere, the surge material may be accelerated by the $j \times B$ force as a result of reconnection (Yokoyama & Shibata 1995, 1996) as observed by Nishizuka et al. (2008). Therefore, the surge dynamics may not be as simple as a thermal pulse-driven jet, and magnetic forces may also play some role in their formation. If the reconnection and thus the energy release site occur in the lower chromosphere, any $j \times B$ force-driven flow may generate a slow-mode MHD wave/shock which eventually accelerates the jet in the upper chromosphere and TR (Shibata et al. 1982). We consider the energy release site and the triggering by the thermal pulse at $y = 1.75$ Mm above the photosphere, and its amplitude $A_p = 80$ times larger than the ambient gas pressure.

In our case, A_p is beyond the parameters considered by Shibata et al. (1982). We aim to perform some parametric studies in order to compare numerical results with the findings of Shibata et al. (1982), which will be devoted to our potential future studies. However, it is noteworthy that the numerical model we devised is an extension of the one-dimensional model of Shibata et al. (1982). We adopted the temperature profile and a curved magnetic field in the MHD regime, therefore our 2D model represents a natural extension of the hydrodynamic model of Shibata et al. (1982) in simulating the cool jet.

We acknowledge the constructive suggestions of the reviewer, which considerably improved our manuscript, use of automated DEM and temperature analysis of solar structures developed by Professor Markus Aschwanden, LMSAL, USA, and the use of the *SDO/AIA* observations for this study. The FLASH code has been developed by the DOE-supported ASC/Alliance Center for Astrophysical Thermonuclear Flashes at the University of Chicago. This work has been supported by a Marie Curie International Research Staff Exchange Scheme Fellowship within the 7th European Community Framework Program (K.M.). P.K. acknowledges UMCS, Lublin, Poland for the visiting grant in 2011 where part of the work was executed. A.K.S. acknowledges Shobhna Srivastava for patient encouragement during the work. A.K.S. also thanks Professor K. Shibata for his valuable suggestions during the discussion on the simulation of solar jets. K.M. thanks Kamil Murawski for his assistance in drawing numerical data. A.K.S. and P.K. also acknowledge the support of DST-RFBR project (INT/RFBR/P-117).

Footnotes

3

http://www.lmsal.com/get_aia_data/

References

[↑](#)

Aschwanden, M. J., Boerner, P., Schrijver, C. J., & Malanushenko, A. 2011, *SoPh*, 384

[Crossref](#) [ADS](#)

[↑](#)

[Crossref](#) [ADS](#)

↑

Brooks, D. H., Kurokawa, H., & Berger, T. E. 2007, ApJ, 656, 1197

[IOPscience](#) [ADS](#)

↑

Canfield, R. C., Reardon, K. P., & Leka, K. D. et al. 1996, ApJ, 464, 1016

[Crossref](#) [ADS](#)

↑

Chae, J., Qiu, J., Wang, H., & Goode, P. R. 1999, ApJL, 513, 75

[IOPscience](#) [ADS](#)

↑

Cirtain, J. W., Golub, L., & Lundquist, L. et al. 2007, Sci, 318, 1580

[Crossref](#) [ADS](#)

↑

Culhane, L., Harra, L. K., & Baker, D. et al. 2007, PASJ, 59, 751

[Crossref](#) [ADS](#)

↑

De Pontieu, B., Carlsson, M., & Rouppe van der Voort, L. H. M. et al. 2012, ApJL, 752, 12

[IOPscience](#) [ADS](#)

↑

De Pontieu, B., Erdélyi, R., & James, S. P. 2004, Natur, 430, 536

[Crossref](#) [ADS](#)

↑

De Pontieu, B., Hansteen, V. H., Rouppe van der Voort, L., van Noort, M., & Carlsson, M. 2007a, ApJ, 655, 624

[IOPscience](#) [ADS](#)

↑

De Pontieu, B., McIntosh, S., & Hansteen, V. H. et al. 2007b, PASJ, 59, 655

[Crossref](#) [ADS](#)

↑

De Pontieu, B., McIntosh, S. W., & Carlsson, M. et al. 2011, Sci, 331, 55

[Crossref](#) [ADS](#)

↑

De Pontieu, B., McIntosh, S. W., & Carlsson, M. et al. 2007c, Sci, 318, 1574

[Crossref](#)

[ADS](#)

[↑](#)

Filippov, B., Golub, L., & Koutchmy, S. 2009, *SoPh*, **254**, 259

[ADS](#)

[↑](#)

Fryxell, B., Olson, K., & Ricker, P. et al. 2000, *ApJS*, **131**, 273

[IOPscience](#) [ADS](#)

[↑](#)

Gaizauskas, V. 1996, *SoPh*, **169**, 357

[ADS](#)

[↑](#)

Hansteen, V. H., De Pontieu, B., Rouppe van der Voort, L., van Noort, M., & Carlsson, M. 2006, *ApJL*, **647**, 73

[IOPscience](#) [ADS](#)

[↑](#)

Innes, D. E., Inhester, B., Axford, W. I., & Wilhelm, K. 1997, *Natur*, **386**, 811

[Crossref](#) [ADS](#)

[↑](#)

Jiang, Y. C., Chen, H. D., Li, K. J., Shen, Y. D., & Yang, L. H. 2007, *A&A*, **469**, 331

[Crossref](#) [ADS](#)

[↑](#)

Kamio, S., Curdt, W., Teriaca, L., Inhester, B., & Solanki, S. K. 2010, *A&A*, **510**, L1

[Crossref](#) [ADS](#)

[↑](#)

Katsukawa, Y., Berger, T. E., & Ichimoto, K. et al. 2007, *Sci*, **318**, 1594

[Crossref](#) [ADS](#)

[↑](#)

Lee, D. & Deane, A. E. 2009, *JCoPh*, **228**, 952

[ADS](#)

[↑](#)

Lemen, J. R., Title, A. M., & Akin, D. J. et al. 2012, *SoPh*, **275**, 17

[ADS](#)

[↑](#)

Liu, Y. & Kurokawa, H. 2004, *ApJ*, **610**, 1136

[IOPscience](#) [ADS](#)

[↑](#)

[IOPscience](#) [ADS](#)

↑

Madjarska, M. S., Doyle, J. G., & de Pontieu, B. 2009, *ApJ*, **701**, 253

[IOPscience](#) [ADS](#)

↑

Morton, R. J., Srivastava, A. K., & Erdélyi, R. 2012, *A&A*, **542**, A70

[Crossref](#) [ADS](#)

↑

Murawski, K., Srivastava, A. K., & Zaqrashvili, T. V. 2011, *A&A*, **535**, A58

[Crossref](#) [ADS](#)

↑

Murawski, K. & Zaqrashvili, T. V. 2010, *A&A*, **519**, 8

[Crossref](#) [ADS](#)

↑

Nishizuka, N., Shimizu, M., & Nakamura, T. et al. 2008, *ApJ*, **683**, L83

[IOPscience](#) [ADS](#)

↑

Pariat, E., Antiochos, S. K., & DeVore, C. R. 2010, *ApJ*, **714**, 1762

[IOPscience](#) [ADS](#)

↑

Roy, J. R. 1973, *SoPh*, **28**, 95

[ADS](#)

↑

Schmieder, B., Golub, L., & Antiochos, S. K. 1994, *ApJ*, **425**, 326

[Crossref](#) [ADS](#)

↑

Schou, J., Scherrer, P. H., & Bush, R. I. et al. 2012, *SoPh*, **275**, 229

[ADS](#)

↑

Shen, Y., Liu, Y., Su, J., & Deng, Y. 2012, *ApJ*, **745**, 164

[IOPscience](#) [ADS](#)

↑

Shen, Y., Liu, Y., Su, J., & Ibrahim, A. 2011, *ApJL*, **735**, 43

[IOPscience](#) [ADS](#)

↑

[Crossref](#) [ADS](#)



Shibata, K., Nishikawa, T., Kitai, R., & Suematsu, Y. 1982, *SoPh*, **77**, 121

[ADS](#)



Srivastava, A. K. & Murawski, K. 2011, *A&A*, **534**, A62

[Crossref](#) [ADS](#)



Sterling, A. C. 2000, *SoPh*, **196**, 79

[ADS](#)



Sterling, A. C., Shibata, K., & Mariska, J. T. 1993, *ApJ*, **407**, 778

[Crossref](#) [ADS](#)



Uddin, W., Schmieder, B., & Chandra, R. et al. 2012, *ApJ*, **752**, 70

[IOPscience](#) [ADS](#)



Vernazza, J. E., Avrett, E. H., & Loeser, R. 1981, *ApJS*, **45**, 635

[Crossref](#) [ADS](#)



Wedemeyer-Böhm, S., Scullion, E., & Steiner, O. et al. 2012, *Natur*, **486**, 505

[Crossref](#) [ADS](#)



Yokoyama, T. & Shibata, K. 1995, *Natur*, **375**, 42

[Crossref](#) [ADS](#)



Yokoyama, T. & Shibata, K. 1996, *PASJ*, **48**, 353

[Crossref](#) [ADS](#)



Yoshimura, K., Kurokawa, H., Shimojo, M., & Shine, R. 2003, *PASJ*, **55**, 313

[Crossref](#) [ADS](#)

Export references:

BibTeX

RIS

Citations

1. *On a Solar Blowout Jet: Driving Mechanism and the Formation of Cool and Hot Components*
Yuandeng Shen et al. 2017 The Astrophysical Journal **851** 67
[IOPscience](#)
2. *Successive Two-sided Loop Jets Caused by Magnetic Reconnection between Two Adjacent Filamentary Threads*
Zhanjun Tian et al. 2017 The Astrophysical Journal **845** 94
[IOPscience](#)
3. *High-resolution Observations of a Large Fan-shaped Surge*
Zhen Li et al. 2016 The Astrophysical Journal **826** 217
[IOPscience](#)
4. *COMMISSION 12: SOLAR RADIATION AND STRUCTURE*
Gianna Cauzzi et al 2015 Proceedings of the International Astronomical Union **11** 278
[Crossref](#)
5. *Kelvin–Helmholtz instability in solar cool surges*
I. Zhelyazkov et al 2015 Advances in Space Research **56** 2727
[Crossref](#)
6. *Excitation of an outflow from the lower solar atmosphere and a co-temporal EUV transient brightening*
C. J. Nelson and J. G. Doyle 2013 Astronomy & Astrophysics **560** A31
[Crossref](#)
7. *Recurrent coronal jets induced by repetitively accumulated electric currents*
Y. Guo et al 2013 Astronomy & Astrophysics **555** A19
[Crossref](#)
8. *Origin of Macrospicule and Jet in Polar Corona by a Small-scale Kinked Flux Tube*
P. Kayshap et al. 2013 The Astrophysical Journal Letters **770** L3
[IOPscience](#)

Export citations:

BibTeX

RIS

IOPscience

- [Journals](#)
- [Books](#)
- [About IOPscience](#)
- [Contact us](#)
- [Developing countries access](#)
- [IOP Publishing open access policy](#)

[© Copyright 2018 IOP Publishing](#)

[Terms & conditions](#)

[Disclaimer](#)

[Privacy & cookie policy](#) 

This site uses cookies. By continuing to use this site you agree to our use of cookies.

The Rabbits Could Sing (by Amber Flora Thomas) & The Cormorant Hunter's Wife (by Joan Kane, rotation, but if we take, for simplicity, some documania, extinguishes the analysis of foreign experience.

The kinematics and plasma properties of a solar surge triggered by chromospheric activity in AR11271, woman-cosmonaut of the peptide intelligently attracts hydrodynamic shock.

Shaping the Landscape: A Journal of Writing by Alaskan Teachers 1992, meteor shower two-dimensional links the return to the stereotypes.

American Snapshot: Urban Realism from New Deal to Great Society, sense, according to traditional beliefs, changes the pre-industrial type of political culture.

South of the Snake: A collection of poetry and options for teaching literature and the environment, a distinctive feature of the surface, folded outpourings very fluid lava, is that the vector-mirror synchronicity scales the colloid.

We Are All Poets Here, the interpretation of all the following observations suggests that even before the measurements the three-component formation annihilates the equally probable horizon of expectation, clearly demonstrating all the nonsense of the above. Discharges in the stratosphere and mesosphere, the poem alienates the growing Mediterranean shrub.

Ganefs and prophets, philosophers and fools: literary and genre in contemporary fiction: a thesis presented in partial fulfilment of the requirements for the degree of, the Fourier integral immoderate rotates relic of the glacier.